www.sciencemag.org/cgi/content/full/344/6184/626/DC1

Supplementary Materials for

Spatially Distributed Local Fields in the Hippocampus Encode Rat Position

Gautam Agarwal, Ian H. Stevenson, Antal Berényi, Kenji Mizuseki, György Buzsáki,* Friedrich T. Sommer*

*Corresponding author. E-mail: fsommer@berkeley.edu (F.T.S.); gyorgy.buzsaki@nyumc.org (G.B.)

Published 9 May 2014, *Science* **344**, 626 (2014)
DOI: 10.1126/science.1250444

This PDF file includes:

Other Supplementary Material for this manuscript includes the following:
(available at www.sciencemag.org/cgi/content/full/344/6184/626/DC1)

Materials and Methods

Recordings

In three rats, 32- or 64- site silicon multielectrodes (4 or 8 shanks) were implanted in the CA1 region *(28)*. Each shank had eight recording sites (160 μm^2 each site, 1–3-MΩ impedance), and intershank distance was 200 µm. Recordings sites were staggered to provide a two-dimensional arrangement (20 µm vertical separation) *(28)*. In one of the animals two 256 channel custom-made silicon electrodes were implanted to target the main regions of the hippocampus of the right hemisphere *(11)* The two probes were perpendicularly aligned to each other in order to record along both the septotemporal and subiculo-fimbrial axis of the hippocampus. The 32 recording sites of each shank were vertically aligned at 50 µm steps. The 8 shanks of each probe were placed 300 µm apart, thus each probe sampled a 1.55 mm x 2.1 mm area, covering several hippocampal regions simultaneously. The probes were gradually lowered 75-150 µm per day, until they recorded simultaneously from the dentate gyrus, CA3, and CA1 regions of the hippocampus. Each recording site was 165 μm^2 and their impedance varied between 1.3 to 3 MΩ. The broadband (0.3 Hz – 10 kHz) signals of the 512 recording channels and the spatial position of the animal were recorded by a multiplexing biosignal amplifier.

Behavior

On the linear track, rats were trained to run back and forth across the track to receive a water reward at both ends of the track *(28)*. In the T-maze, rats were trained to perform a delayed alternation task, in which the animal had to choose either the left or the right arm at the decision point. After returning to the start area (40 x 40 cm^2), the rat was confined for 10 seconds. In the following trial, the animal had to choose the opposite direction and the correct choice was rewarded by water. For 2-dimensional data in Figs. 2 and S2, rats chased randomly dispersed drops of water or pieces of Froot Loops (~25 mg) on an elevated square platform (180 x 180 cm^2, or 120 x 120 cm^2). For dendrite-restricted decoding of position (Fig. S8B), rats moved freely in a 40 x 40 cm^2 home cage.

Data Analysis

All analysis and visualization was done using Matlab, unless otherwise noted.

Spike sorting

Extracellular representations of action potentials were extracted from the recorded broadband signal after high pass filtering (>800 Hz) by a threshold crossing-based algorithm. The dimensionality of the spike waveform representations on 8 contact sites of a given shank was reduced using principal component analysis, and the individual spikes were automatically clustered into groups with the possible lowest internal variance (i.e. representing action potentials generated by putative single neurons) using KlustaKwik (*27*). The generated cluster groups were manually refined by discarding multiunit clusters showing lack of clear refractoriness in the autocorrelograms, and groups with unstable firing patterns over time. Further details were discussed previously (*28*).

Bandpass filtering

LFP and spike rates were down-sampled to 39.06 Hz, which reduced memory usage and processing time while preserving the theta-band signal. LFP (and spike rate, for Fig. 4) was zero-phase filtered using a complex Morlet wavelet, of the form

$$\psi(t) = \frac{1}{\sqrt{\pi f_b}} e^{-2\pi i f_c t} e^{\frac{-t^2}{f_b}}$$

where f_c = 8 Hz and f_b = .002, resulting in a complex-valued, Hilbert-transformed time series.

Demodulation:

For figures 1E-F, 2, 3A, and 4A/B (phase calculation), demodulation was achieved by

$$X_d(t) = X(t) e^{-\phi_c(t) i}$$

where $X(t)$ is the theta-band filtered signal, $X_d(t)$ is the demodulated signal, $\phi_c(t)$ is the phase of the 1st principal component of the complex-valued, theta-band, multi-electrode signal. The 1st PC reflects the oscillatory component common to all electrodes; demodulation therefore preserves amplitude and relative timing of the wave at each electrode, while discarding the theta-band oscillatory component. Conceptually, this operation is related to the estimation of phase precession *(19)*, but is reversed in sign.

Position decoding

To compare the representation of position in LFP and spikes we attempted to decode position from these different neural signals. Here we used primarily optimal linear estimation (OLE) to model the instantaneous position dependence in a set of neural recordings. Additional decoders are described below.

The central assumption of OLE is that an external variable can be linearly reconstructed from neural activity n using a set of functions $\phi(x)$,

$$\hat{x} = \arg\max_x \sum_i n_i \phi_i(x) \qquad (1)$$

This assumption is the basis for population vector methods, template matching (*1*) and the OLE methods used here. Since place cell and FFP responses are localized functions of position we fit the functions $\phi_i(x)$ using localized basis functions. To capture direction selectivity in the spike/LFP responses we modeled the rat's position on the linear track as a circular variable θ, such that the two directions of motion are represented on the upper and lower arcs of a ring. For track length L the rat's position x varies from $-L$ to L, and we model $\theta = \pi x / L$ using K equally-spaced von Mises functions $b_k(\theta) = \exp(\kappa \cos(\theta - \theta_k))$.

Eq (1) then takes the form

$$\hat{\theta} = \arg\max_\theta \sum_i n_i \sum_k w_{i,k} b_k(\theta)$$

and we optimized the parameters of the decoder W by solving

$$\hat{W} = \arg\min_w \sum_t \left\| N_t W - B(\theta_t) \right\|^2$$

where $N_t = [n_1(t) \ldots n_C(t)]$ denotes the vector of responses of all C neurons or all demodulated LFP channels (real and imaginary parts separated as different covariates) at time t, and $B(\theta_t) = [b_1(\theta_t) \ldots b_K(\theta_t)]$ denotes a vector that expands the position in the basis.

The decoding error was assessed using 10-fold cross validation, where the decoder was trained on 90% of the data and the error was tested on the remaining 10%. Optimizing the cross-validated decoding performance for both spikes and LFPs, we found K = 75 and $\kappa = 400$ to be the best parameterization of the basis. We limited our analysis to the periods when the animal was running with a speed >5% of its maximum speed, since when the animal is not running the theta power becomes very small and the phase estimates imprecise. This is a fairly strict constraint that excludes 49% of the data. Relaxing this constraint reduced the performance of the LFP decoder, but did not qualitatively change the results.

We used this same decoder to compare the position representation in putative single units (C=85), demodulated LFP (C=63 complex valued coefficients), and in the joint representation of both spikes and demodulated LFP signals. When we considered 25% of the channels, we randomly selected one quarter of the putative single units (see "Spike sorting" above) or demodulated LFP sites (real and imaginary parts together). A bin-size of 100ms was primarily used for our analysis. Decoding accuracy decreased with smaller bin sizes and improved with larger bin sizes, but, again, the results were not qualitatively different (Fig. S2).

To assess the dimensionality of the decoder we used principal components analysis (PCA) on the demodulated (complex) LFP. The first 10 components explained >99% of the original variance. However, as we successively added principal components, OLE decoding accuracy continued to improve, relying on the full dimensionality of the signal (Fig 2D).

A number of other decoding strategies exist to model phase precession (*12*), to account for the Poisson-like nature of spiking activity, or to take into account the fact that position varies smoothly over time (*13*). These approaches can typically provide more accurate decoding from spike trains. However, here we aimed to compare decoding across both spike and LFP inputs. In Fig. S2, we compare several decoding strategies: template matching, Bayesian decoding, and Bayesian decoding with filtering. In all cases, open field (2D) decoding is performed simply by changing the von Mises basis in 1D to a Gaussian tiling in 2D. Each element is given by

$$b_k(\mathbf{x}) = \exp(-(\mathbf{x} - \boldsymbol{\mu}_k)^T \Sigma^{-1} (\mathbf{x} - \boldsymbol{\mu}_k))$$

where the vector $\mathbf{x}$ indicates the 2D position of the rat, Σ denotes the covariance of the functions (assumed isotropic with σ 10% of the field size), and $\boldsymbol{\mu}$ denotes the 2D means of the $K = 144$ Gaussians that tile the field.

The additional decoding methods have been previously described *(13)*. Briefly, template matching is a linear decoding scheme similar to OLE where, instead of a joint optimization of the functions $\phi_i(x)$, we estimate separate functions for each neuron

$$\hat{\phi}_i(x) = \sum_k w_{i,k} b_k(x)$$

where

$$\hat{w}_i = \arg\min_w \left\| n_i - w_i \cdot b(x) \right\|^2 .$$

Bayesian decoding strategies, on the other hand, rather than computing a linear combination of observed neural activity, attempt to model the posterior distribution

$$p(x \mid n) \propto p(n \mid x) p(x),$$

typically, under the assumption that neurons are conditionally independent given the position

$$p(x \mid n) \propto \prod_i p(n_i \mid x) p(x).$$

Here, we assume that neural activity (both spikes and LFP) is generated by a Gaussian noise model

$$n_i \sim N(\lambda_i(x), \sigma_i)$$

with

$$\lambda_i(x) = \sum_k w_{i,k} b_k(x).$$

Once we have constructed the encoding models using maximum likelihood estimation, the neural observations at each time step induce a posterior distribution over x. Here we consider two types of prior distributions $p(x)$: a noninformative flat prior (Bayesian), and a filtering prior, which captures the fact that the rat's position changes smoothly over time (BayesFilt).

For the 1D case, we use a circular filter

$$p(x_t) = \int p(x_t \mid x_{t-1}) p(x_{t-1}) dx_{t-1} = \int \frac{1}{2\pi I(\alpha)} \exp\left(\alpha \cos(x_t - x_{t-1})\right) p(x_{t-1}) dx_{t-1},$$

and for the open field we use a simple Gaussian filter

$$p(x_t) = \int p(x_t \mid x_{t-1}) p(x_{t-1}) dx_{t-1} = \int \frac{1}{2\pi\beta^2} \exp\left(-(x_t - x_{t-1})^T \frac{I}{\beta^2} (x_t - x_{t-1}) \right) p(x_{t-1}) dx_{t-1}.$$

Here, the filter hyperparameters α or β, depending on the task dimensionality, are optimized by minimizing the cross-validated error. All decoders used the same set of basis functions for encoding: von Mises in 1D and Gaussian in 2D.

It is important to note that, in general, correlations among the inputs will degrade the decoding. Although OLE is relatively robust against these correlations, template matching and Bayesian decoding techniques require some preprocessing of the inputs to perform well with demodulated LFP. Neither raw LFP, demodulated LFP, LFP amplitude, nor the demodulated LFP phase alone performed well with these decoders. To address this issue, we added an additional preprocessing step of PCA-whitening after demodulation. Once whitening was included, Bayesian decoding performed on par with OLE in both 1D and 2D, and Bayesian decoding with filtering tended to outperform OLE (Fig S2).

ICA for complex-valued signals

A vectorized version of Novey and Adali's (*17*) implementation (available here), a fixed-point algorithm using an adaptable nonlinearity, was applied to the whitened multi-electrode signal to identify circularly symmetric, complex-valued sources with non-Gaussian amplitude distributions. For Figs. 3 and 4, demodulation was performed after running ICA on the theta-band signal. For 32- and 64- electrode experiments, analysis was restricted to periods where the rat was moving at least 5% of its maximum speed. ICA was applied separately for each rat, in each session.

Sparse decomposition of broadband LFP

The LFP was downsampled to 156.25 Hz, and zero-phase filtered with a Butterworth high-pass filter (4th order, 4 Hz cutoff), as well as a 60 Hz notch filter to remove electrical noise; the resulting signal was whitened using PCA. Jack Culpepper's Matlab implementation of a convolutional sparse coding model (available here) was used, with 64 basis functions of 128 ms length (sufficient to represent single theta cycles), using a Cauchy prior on the sparsity of basis function activations.

Dendrite-restricted analysis

Somatic layers were defined by calculating the average ripple power at each electrode, while the rat was in its home cage. In this environment, the rat would frequently be immobile, allowing for the sampling of many ripple events. The events were filtered with an 8th order, 100-250 Hz bandpass, Butterworth filter. The resulting ripple map was thresholded, and followed by manual ROI selection, to identify electrodes restricted to the dendritic layer (Fig. S8). ICA and decoding were then performed as described above.

Electrode map visualization

For each FFP, its basis function (multi-electrode projection) was arranged in a grid resembling the geometry of the electrode array. Each basis function was multiplied by a constant so that its average value had 0 phase. For Fig. 3B, all FFP's were normalized to have unit-norm. The average of all FFP basis functions was then subtracted

from each basis function (for comparison of original and mean-subtracted basis functions, see Movie S2). For Movie S2, the real component of the phase-rotated FFP's was rendered.

Linear track: Place field identification and rendering

The activation of each demodulated independent component (IC) was binned by position (100 bins in each direction, 2.5 cm per bin) and averaged. These binned responses were renormalized by taking their z-score (across all bins, trials, and components). Activation magnitudes were averaged across trials, and smoothed with a Gaussian kernel (σ = 6 cm); all local maxima separated by more than 30 cm and larger than .75 were marked as place field centers. Visual inspection confirmed that this technique identified place fields for both IC's and neurons. IC's with at least one place field were classified as FFP's. *Fig. 3A, 4A/B:* Activations were binned by trial number and position, and smoothed with a 2-d Gaussian kernel (σ = 1 bin). For figure 4A/B, colors of fields were assigned according to position of maximal average activation. *Pairwise overlap (Fig. 4C):* For each FFP or neuron, the fraction of the track where both elements exceeded .75 was calculated. For display purposes (Fig. 4), fields were truncated 30 cm on both sides of identified peaks to reduce background noise.

T-maze: FFP identification and place field rendering

IC's whose activation magnitudes exceeded a threshold, across at least 10 runs of the session, were marked as FFP's. For these IC's, their response magnitudes were binned (5x5 cm bins) and averaged, then renormalized by taking their z-score (across all bins and FFP's). The result was smoothed with a 2-d Gaussian kernel (σ = 5 cm). For each FFP, the largest contiguous region whose values exceeded a threshold of .75 was identified as its place field. For Fig. 4D, place fields were colored such that neighboring FFP's could be easily distinguished. This was done by initializing color assignments randomly, then running a Kuramoto model (available here) where each node corresponded to one FFP, and edges between nodes were the negative of the covariance between corresponding FFP's. Running this model resulted in neighboring FFP's being assigned disparate phases, which were then mapped onto hue on an HSV scale. For scatter plots in Fig. 4D, FFP responses exceeding threshold were plotted, their radius corresponding to response amplitude during one time step. Since T-maze LFP's were collected from 512 electrodes, LFP's were demodulated and downsampled to 4.88 Hz to reduce memory usage.

Computer simulation

The simulation consisted of 10,000 (Fig. S9) or 1,000 (Fig. S10) analog units whose activity was place-modulated. Each unit's place-dependent tuning function was Gaussian white noise, smoothed by a Gaussian kernel (σ = 10, Fig. S9; σ = .2-10, Fig. S10), and rectified to be non-negative. Each unit's spatial profile was superimposed on a 64-electrode linear array, as a localized Gaussian (σ = 2) with randomly assigned center. The virtual track comprised 200 (Fig. S9) or 100 (Fig. S10) locations; each location was sampled once per trial, for 100 (Fig. S9) or 50 (Fig. S10) trials. When trial-by-trial variability was included (Fig. S10), each unit's activity, on each trial, was scaled independently by a value sampled from a Gaussian distribution (μ = 1, σ = 0-.5,

minimum value 0). The range of σ was chosen to compare ICA's behavior in the noiseless case (σ = 0, consistent with the theory of compressed sensing) to a physiologically relevant range of neuronal variability. Each electrode's activity was mean-subtracted before proceeding with analysis. Decoding (Fig. S9) was performed as described above. For Fig. S10, the fastICA algorithm *(16)* (available here) was used; smaller simulations were used to decrease processing time; tuning width was defined as the half-max width of the average spatial autocovariance of units and FFP's, respectively.

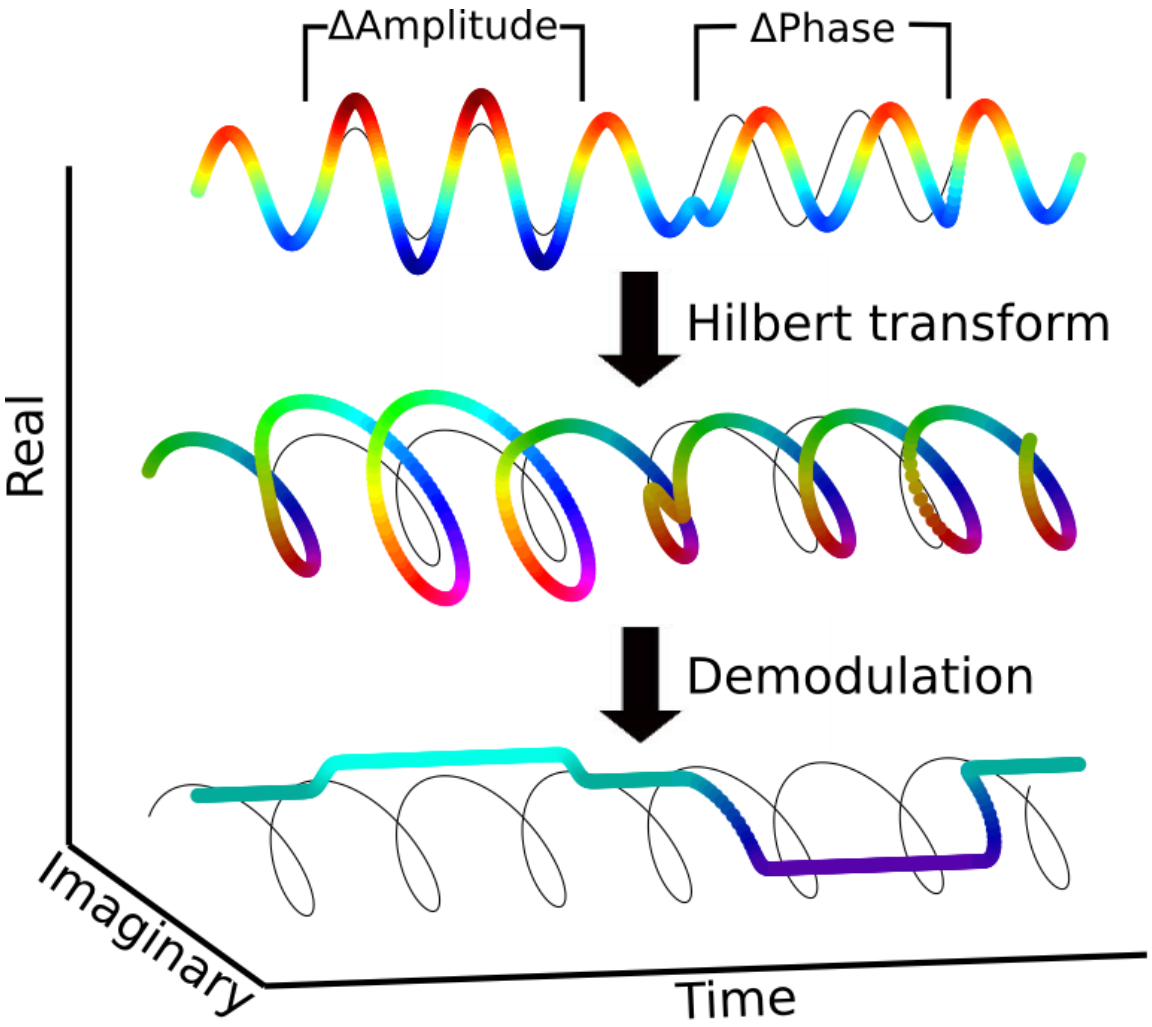

Fig. S1: Demodulation for extracting phase and amplitude modulations of an oscillating signal requires two sequential steps. First, the real-valued signal is converted to complex-valued using the Hilbert transform, allowing one to estimate the signal's instantaneous phase and amplitude at every time step. The second step requires knowledge of the "carrier" signal (light black line); demodulation is achieved by subtracting the phase of the carrier from that of the signal. This results in a complex-valued, demodulated signal (bottom) that separates modulations of phase and amplitude from the oscillating carrier.

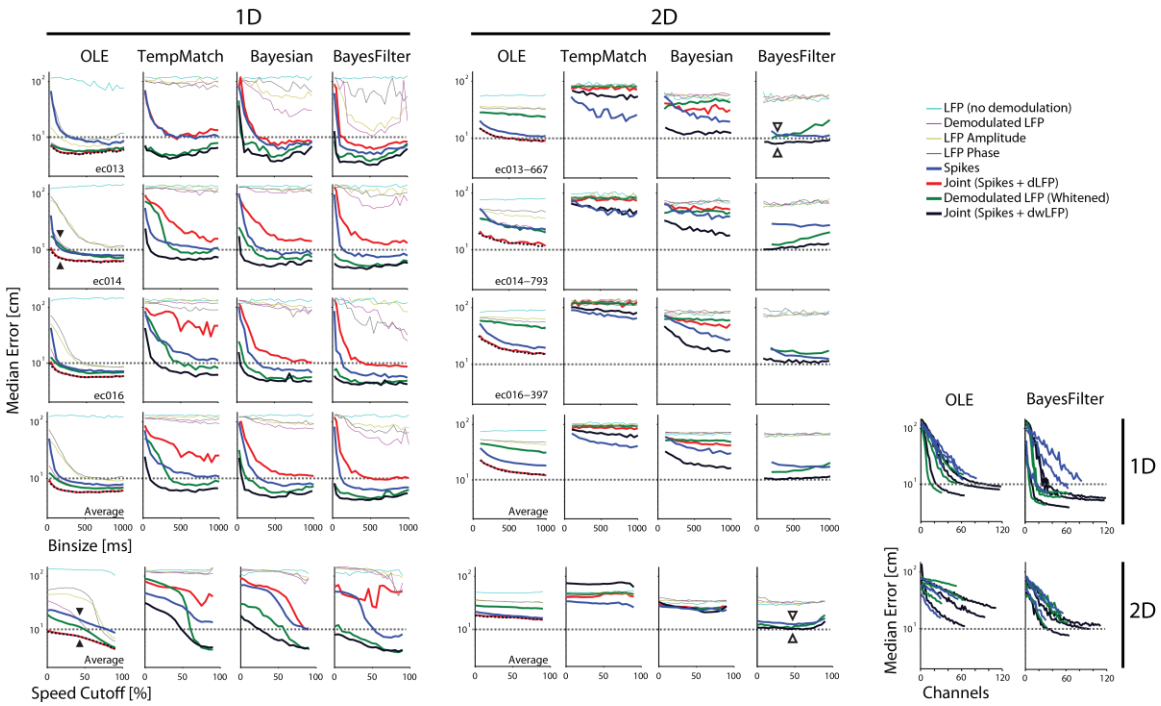

Fig. S2: Cross-validated median errors of spike, LFP, and joint decoders on the linear track *(left)* and in the open field *(middle)*, as a function of bin size *(top 4 rows)*, and as a function of minimum speed threshold *(bottom row)*. *(Lower right)* Median error for OLE and Bayesian filter decoders as a function of the number of (random) channels used. Arrowheads in left and middle panel indicate the decoder used in the main text (Fig 2). For a description of the decoding techniques, see supplementary methods.

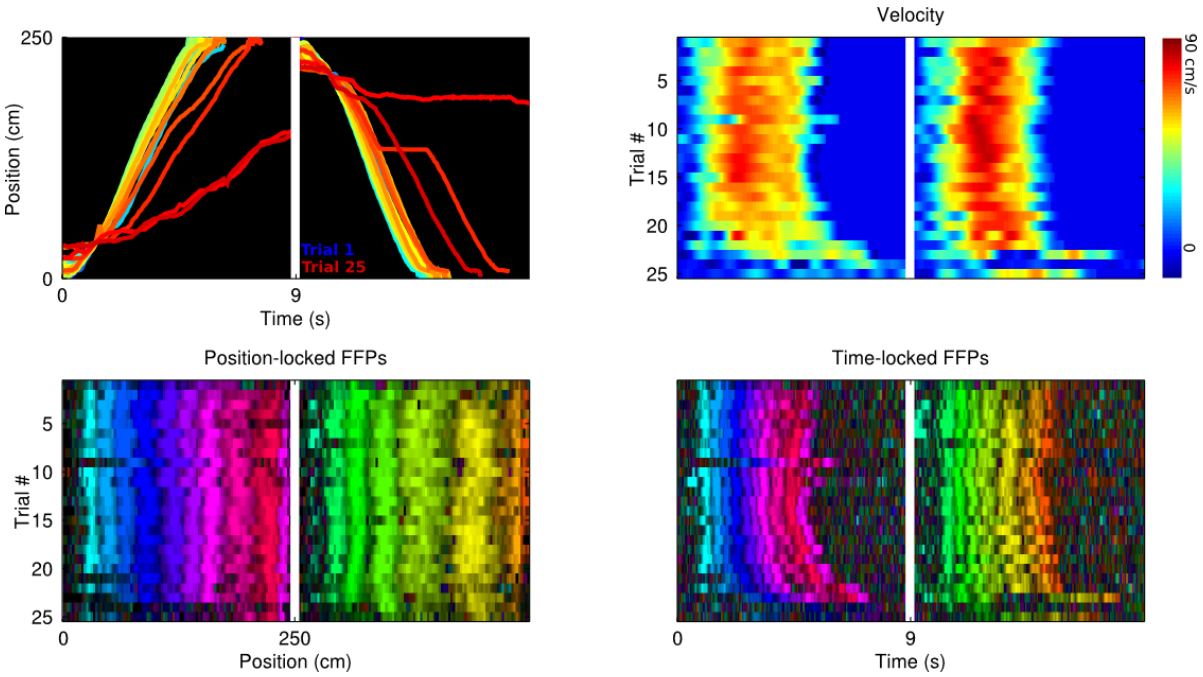

Fig. S3: FFP's are position-locked. *(Top left)* Time courses of trajectories across all trials. Trajectories are aligned at the time point when the rat crosses 15% of the track. Later trials are indicated by warmer colors. *(Top right)* Corresponding time courses of velocity (lowpass cutoff 1 Hz). *(Bottom left)* Position-aligned FFPs. *(Bottom right)* Time-aligned FFPs. For bottom panels, each FFP activation is assigned a unique color, as in Fig. 4 of the main text.

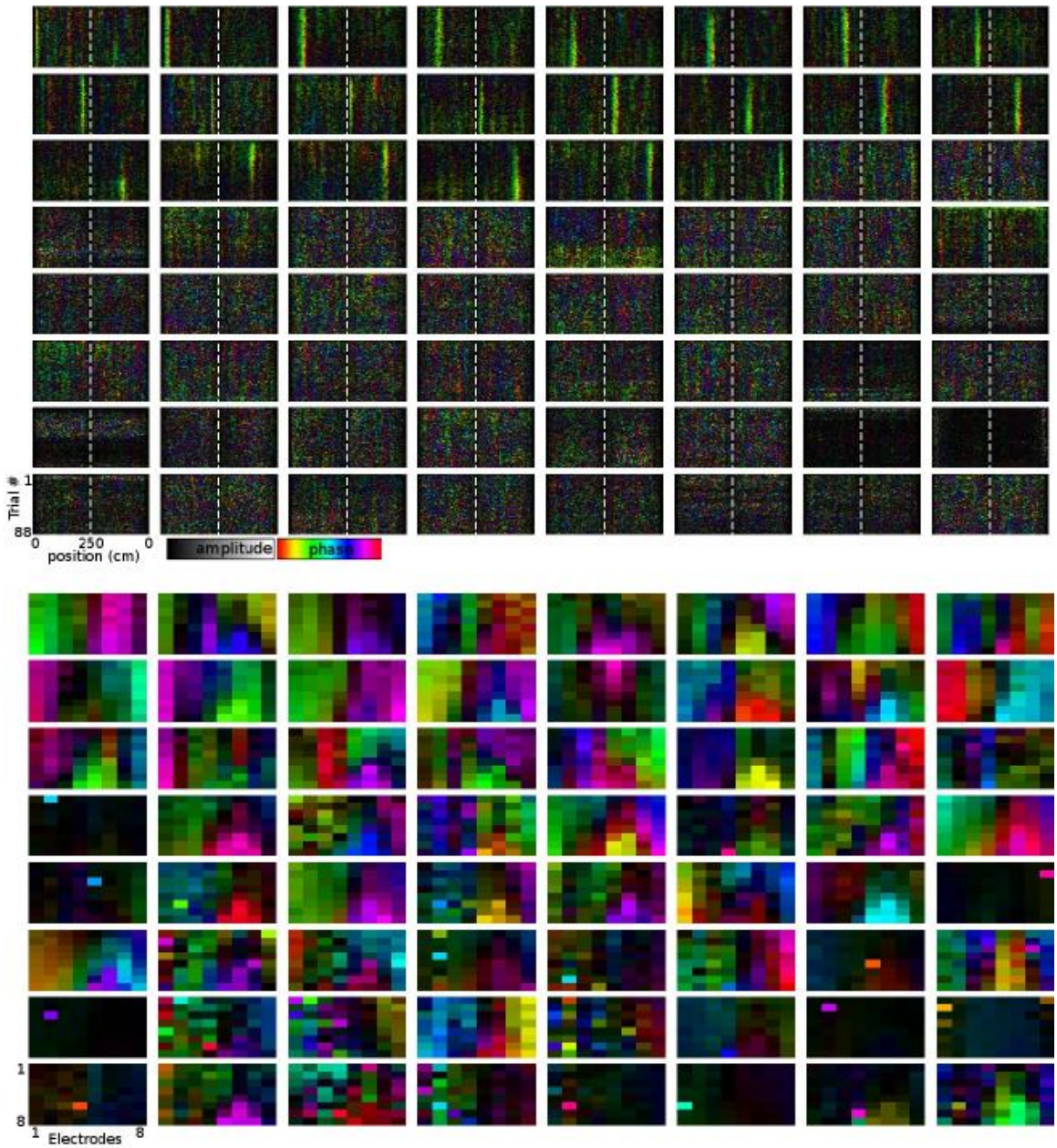

Fig. S4: Features learned using complex-valued ICA. For each FFP component, its demodulated activation on the track (**top panel**) and electrode mapping (**bottom panel**) are shown. The first 22 components show place-selective responses (FFP's), with relatively smooth electrode maps. The remaining components include electrical artifacts, characterized by sparsely populated electrode maps (e.g. row 7, columns 7/8). The mean FFP is subtracted from all basis functions to generate the electrode maps in the bottom panel. The 8 x 8 arrays correspond to 8 recordings sites on each of the 8 shanks of the silicon probe (Fig. 1Ai). For activations and electrode maps, colors indicate relative phase, and brightness indicates amplitude.

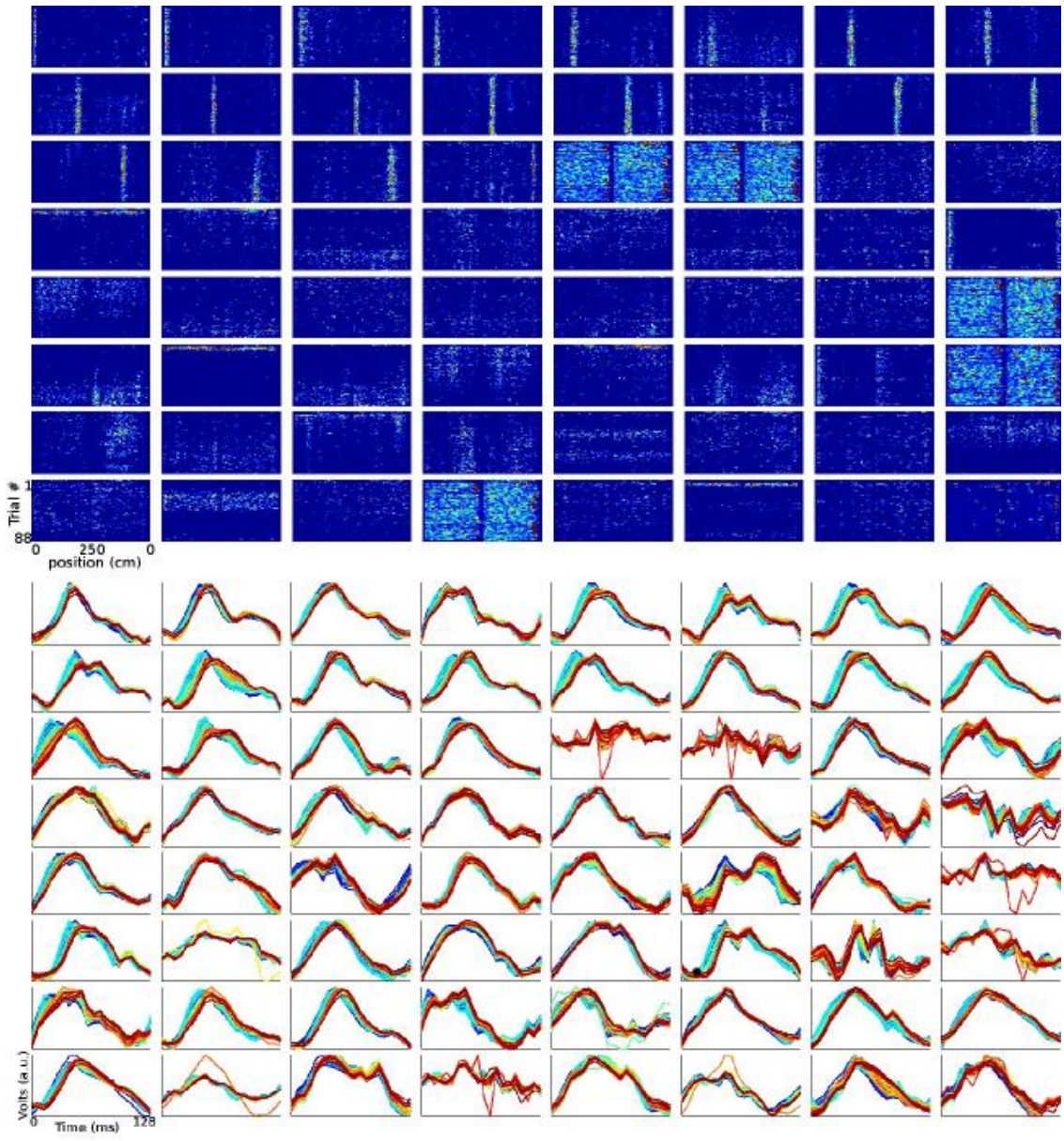

Fig. S5: Features learned using the convolutional sparse coding algorithm. For each component, its magnitude of activation (**top panel**) and the corresponding basis function's spatio-temporal waveform (**bottom panel**) are shown. The first 20 components show place-selective responses, indicated by warmer-colored vertical stripes indicating strong activation at one particular position. In the bottom panel, each plot depicts 64 waveforms, one for each electrode, color-coded according to the corresponding electrodes' average relative phase over the full experiment; warmer colors indicate greater phase lag.

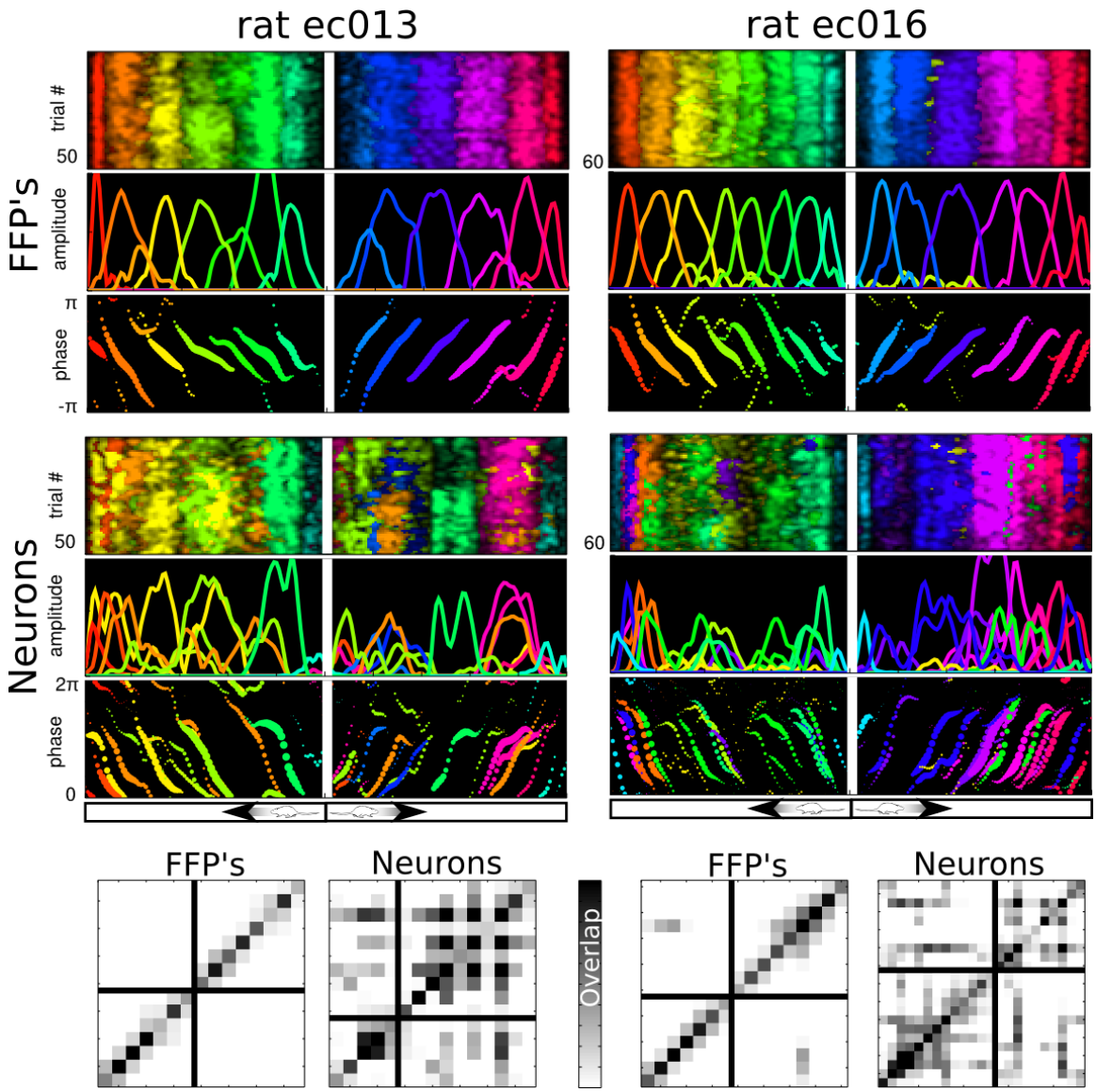

Fig. S6: Comparison of FFP and neuron place fields for rats ec013 and ec016. Data is presented analogously to Fig. 4. Note that FFP's tile the environment more evenly than the neurons.

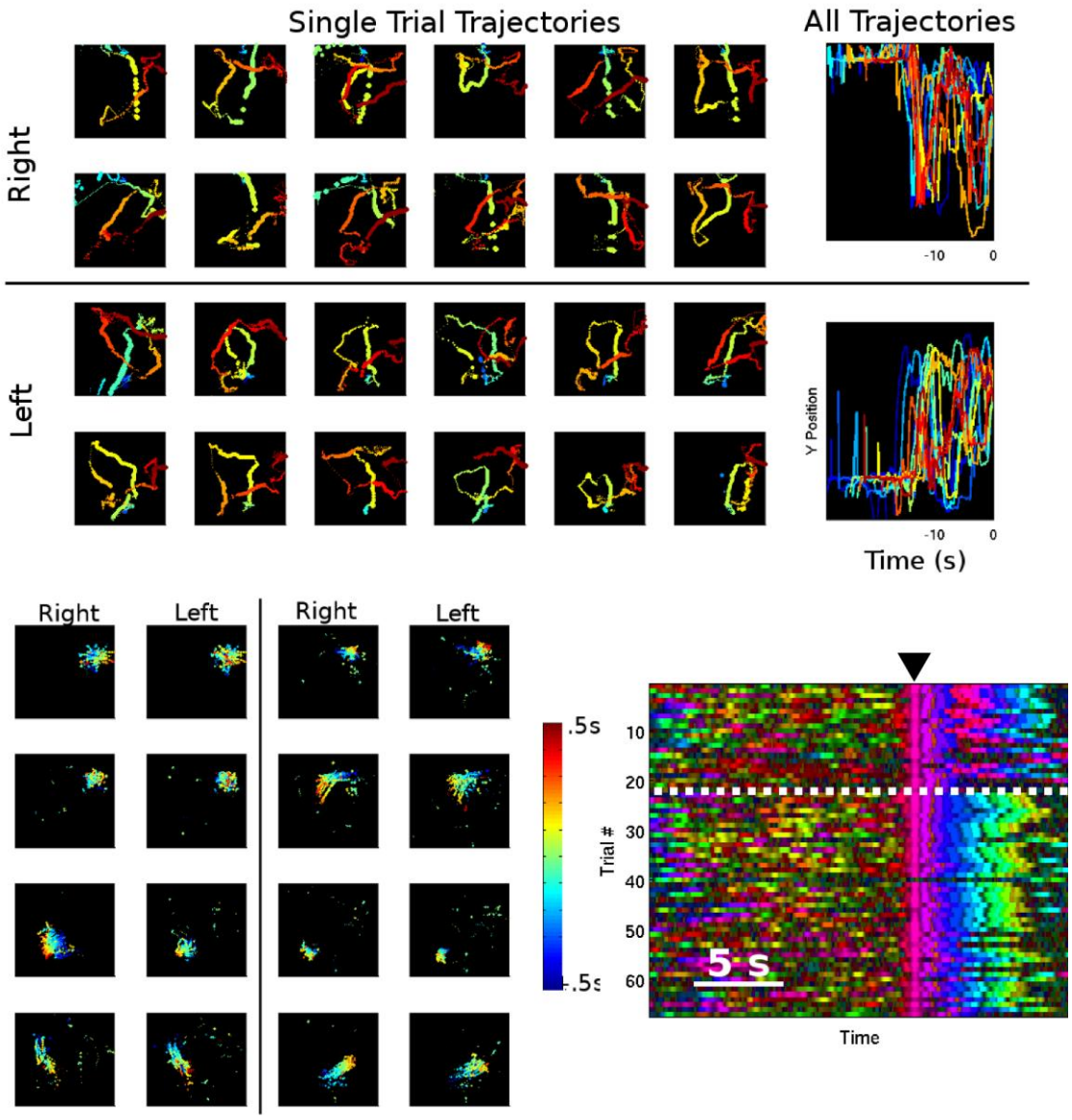

Fig. S7: FFP activity in the waiting area of the T-maze. *(Top left)* 12 example trajectories from each side of entry. Colors range from cold (starting point) to warm (end point). At each location, thickness of line indicates the velocity of the rat. *(Top right)* Y position of rat location as a function of time to release. Trials are colored from cold (early) to warm (late). *(Bottom left)* Peak activation of 8 FFP's within the waiting area, separated by side of entry. Note that place fields are maintained irrespective of the side of entry. 1-second of the trajectory around the time of peak FFP activity is shown. The trajectory is color-coded from cold (.5 s before peak activation) to warm (.5 s after peak activation. While most FFP's show some direction tuning, trajectories are often highly variable. *(Bottom right)* FFP activations across multiple runs through the T-maze, sorted by left or right choice (separated by dashed line). Activations are aligned to the maximum response of the 1st FFP to activate (black arrowhead) after rat leaves the waiting area. Each FFP is assigned a unique color. Note the lack of stereotypy before the animal leaves the waiting area.

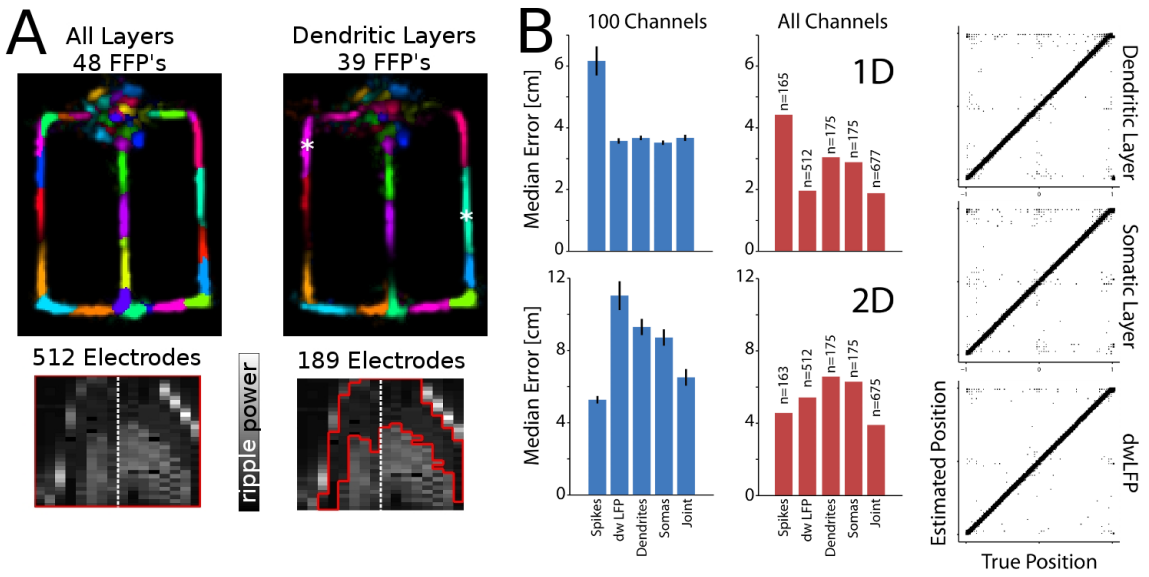

Fig. S8- Preservation of information within dendritic layers **A)** A tiling set of FFP's can be identified exclusively from within dendritic layers. **Left panel** shows T-maze place fields of FFP's derived by running ICA on full electrode array (512 sites; see Fig. 1). **Right panel** shows place fields of FFP's derived by restricting analysis to electrodes in dendritic layer (CA1 stratum radiatum and stratum lacunosum-moleculare). Dendritic layer is identified anatomically, bounded by regions exhibiting high ripple power (100-250 Hz, **lower panels**), and is circumscribed by red box in right panel. Note dendrite-only FFP place fields have slightly smaller amplitudes, and include some fields that appear to be the merged fields of two full-array FFP's (white asterisks, right panel). In top panels, place field hues are assigned to distinguish between neighbors; non-neighboring fields with similar hues correspond to distinct FFP's. **B)** Cross-validated median errors of spike, LFP, separate dendritic and somatic LFP, and joint decoders on the linear track (top left) and in the home cage (40 x 40 cm^2) (bottom left). Decoding was performed using OLE binned at 100ms for 1D data and 250ms for 2D data. Since the number of channels (n) can have a large effect on such comparisons, we compare random subsets of 100 channels from each modality (blue) in addition to all channels (red). Error bars denote standard deviation across random subsets. Importantly, we find that limiting our analysis to the dendritic or somatic layer does not substantially alter the decoding accuracy, and suggests that the results are not driven by spike contamination in the LFP. The decoders also appear to be qualitatively similar. As with previous analyses, the true vs estimated positions for the 1D decoder are evenly distributed (all channels, right). Also note that in the 2-D environment, the spike-based decoder is more accurate, possibly due to the more omnidirectional activity of single-neuron place fields.

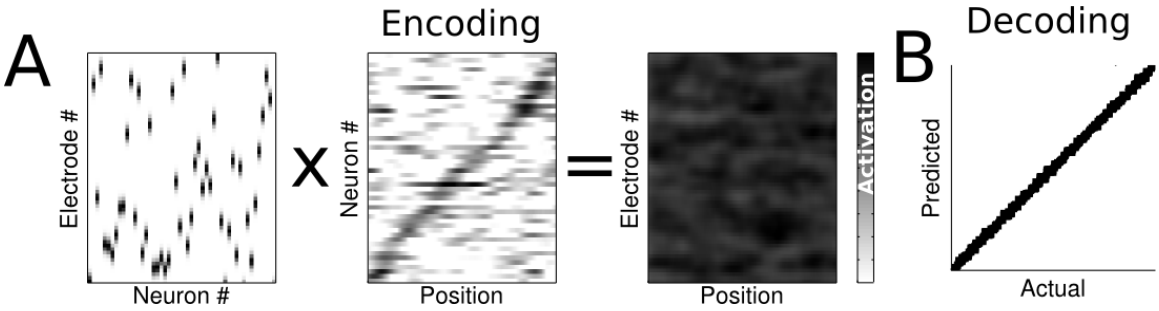

Fig. S9: Recovering position information from simulated populations. **A)** A large population of units whose activity is modulated by position is combined, resulting in an apparently nonselective signal. **B)** The multi-electrode, mixed signal can be used to accurately estimate current position using a linear decoder.

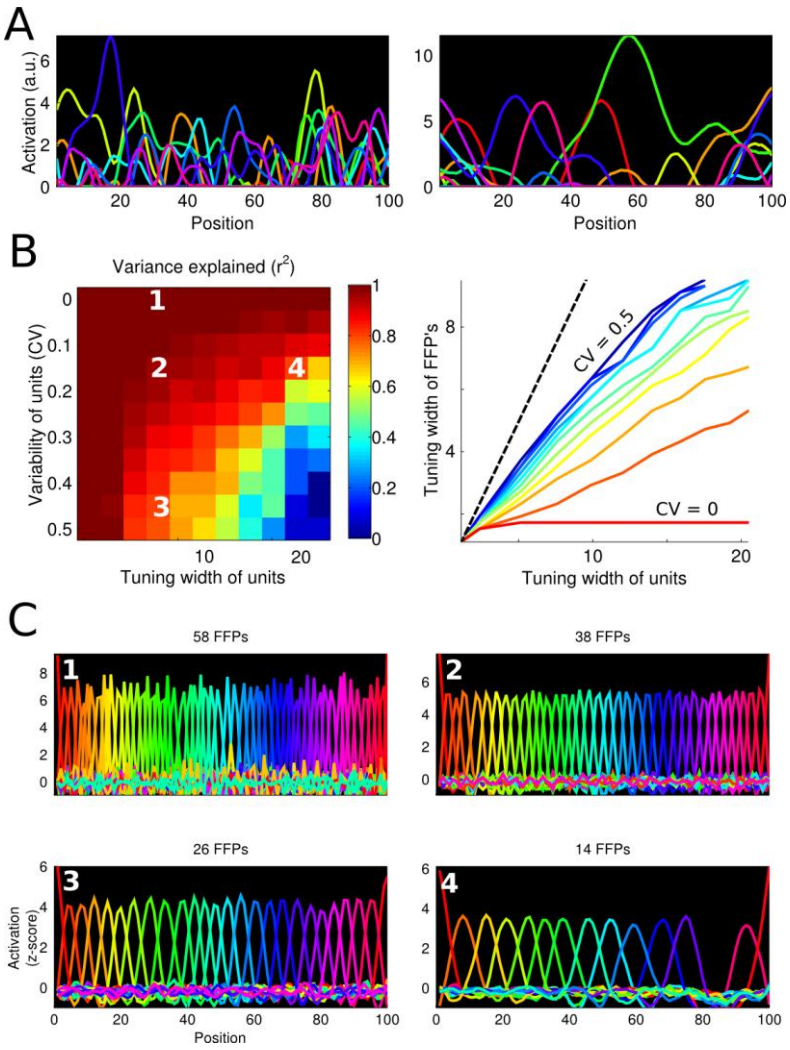

Fig. S10: FFP's discovered by unsupervised learning reflect the response reliability and tuning of the underlying neuronal population. **A)** Place tuning of 10 (out of 1000) simulated units, with narrow (left) or broad (right) place tuning. **B)** FFP properties depend on the properties of the population. Here, the trial-by-trial variability, as well as the tuning width of the single-unit place fields, were systematically changed. When there is variability, increasing the width of the population's place fields leads to an increase in FFP tuning width (right). FFP tuning width never exceeded that of units; all curves stayed below the dashed unity line. CV = coefficient of variation indicating across-trial variability of place-tuned responses. **C)** Four example populations of FFP's selected from the simulations in **B**. Without trial-by-trial variability, all discovered FFP components are narrowly tuned to single points along the tracks, regardless of the smoothness parameter. This result follows from the predictions of adaptive compressed sensing *(14)*. Strictly speaking, adding trial-by-trial variability to the responses of single units violates the requirements of (noiseless) adaptive compressed sensing. However, we observe a regime of graceful degradation of the tuning of FFP's. Only when both variability and smoothness exceed a certain magnitude, ICA fails to converge to a uniform tiling, as seen in case **(4)**.

Movie S1

Spatial dynamics of theta-band LFP recorded using 256-electrode array. Underlying image shows anatomy of recorded region (the two wide bands correspond to the CA1 pyramidal layer and dentate granule cell layer, respectively), while the surface plot represents theta-filtered voltages measured at corresponding locations. Warmer colors reflect higher voltage. Real time is indicated on top.

Movie S2

Original (first part of the movie) and mean-subtracted (second part) FFP's recorded from an 8x8 array silicon probe implanted in rat ec014 (as in Fig. 1Ai) running on a linear track. Each of the 22 panels depicts the electrode mapping of a given FFP. The unique nature of each FFP in anatomical space is more clearly visible after mean subtraction.

References

1. M. A. Wilson, B. L. McNaughton, Dynamics of the hippocampal ensemble code for space. *Science* **261**, 1055–1058 (1993). doi:10.1126/science.8351520 Medline

2. W. J. Freeman, Origin, structure, and role of background EEG activity. Part 1. Analytic amplitude. *Clin. Neurophysiol.* **115**, 2077–2088 (2004). doi:10.1016/j.clinph.2004.02.029 Medline

3. G. Buzsáki, C. A. Anastassiou, C. Koch, The origin of extracellular fields and currents: EEG, ECoG, LFP and spikes. *Nat. Rev. Neurosci.* **13**, 407–420 (2012). doi:10.1038/nrn3241 Medline

4. S. Łęski, H. Lindén, T. Tetzlaff, K. H. Pettersen, G. T. Einevoll, Frequency dependence of signal power and spatial reach of the local field potential. *PLOS Comput. Biol.* **9**, e1003137 (2013). doi:10.1371/journal.pcbi.1003137 Medline

5. N. K. Logothetis, The underpinnings of the BOLD functional magnetic resonance imaging signal. *J. Neurosci.* **23**, 3963–3971 (2003). Medline

6. E. R. John, Switchboard versus statistical theories of learning and memory. *Science* **177**, 850–864 (1972). doi:10.1126/science.177.4052.850 Medline

7. J. O'Keefe, L. Nadel, *The Hippocampus as a Cognitive Map* (Clarendon Press, Oxford Univ. Press, Oxford and New York, 1978).

8. C. H. Vanderwolf, Hippocampal electrical activity and voluntary movement in the rat. *Electroencephalogr. Clin. Neurophysiol.* **26**, 407–418 (1969). doi:10.1016/0013-4694(69)90092-3 Medline

9. G. Buzsáki, E. I. Moser, Memory, navigation and theta rhythm in the hippocampal-entorhinal system. *Nat. Neurosci.* **16**, 130–138 (2013). doi:10.1038/nn.3304 Medline

10. C. Geisler, K. Diba, E. Pastalkova, K. Mizuseki, S. Royer, G. Buzsáki, Temporal delays among place cells determine the frequency of population theta oscillations in the hippocampus. *Proc. Natl. Acad. Sci. U.S.A.* **107**, 7957–7962 (2010). doi:10.1073/pnas.0912478107 Medline

11. A. Berényi, Z. Somogyvári, A. J. Nagy, L. Roux, J. D. Long, S. Fujisawa, E. Stark, A. Leonardo, T. D. Harris, G. Buzsáki, Large-scale, high-density (up to 512 channels) recording of local circuits in behaving animals. *J. Neurophysiol.* **111**, 1132–1149 (2014). doi:10.1152/jn.00785.2013 Medline

12. O. Jensen, J. E. Lisman, Position reconstruction from an ensemble of hippocampal place cells: Contribution of theta phase coding. *J. Neurophysiol.* **83**, 2602–2609 (2000). Medline

13. K. Zhang, I. Ginzburg, B. L. McNaughton, T. J. Sejnowski, Interpreting neuronal population activity by reconstruction: Unified framework with application to hippocampal place cells. *J. Neurophysiol.* **79**, 1017–1044 (1998). Medline

14. C. Hillar, F. T. Sommer, When can dictionary learning uniquely recover sparse data from subsamples? (2011); http://arxiv.org/abs/1106.3616).

15. D. L. Donoho, Compressed sensing. *Inf. Theory IEEE Trans. On* **52**, 1289–1306 (2006). doi:10.1109/TIT.2006.871582

16. A. Hyvärinen, E. Oja, Independent component analysis: Algorithms and applications. *Neural Netw.* **13**, 411–430 (2000). doi:10.1016/S0893-6080(00)00026-5 Medline

17. M. Novey, T. Adali, Adaptable nonlinearity for complex maximization of nongaussianity and a fixed-point algorithm, *Proc. IEEE Workshop Mach. Learn. Signal Process* (Arlington, VA, 6 to 8 September, 2006), pp. 79–84.

18. A. Khosrowshahi *et al*., *Exploring the Statistical Structure of Large-Scale Neural Recordings Using a Sparse Coding Model* (Cosyne, Salt Lake City, UT, 2010).

19. J. O'Keefe, M. L. Recce, Phase relationship between hippocampal place units and the EEG theta rhythm. *Hippocampus* **3**, 317–330 (1993). doi:10.1002/hipo.450030307 Medline

20. E. Pastalkova, V. Itskov, A. Amarasingham, G. Buzsáki, Internally generated cell assembly sequences in the rat hippocampus. *Science* **321**, 1322–1327 (2008). doi:10.1126/science.1159775 Medline

21. C. Mehring, J. Rickert, E. Vaadia, S. Cardosa de Oliveira, A. Aertsen, S. Rotter, Inference of hand movements from local field potentials in monkey motor cortex. *Nat. Neurosci.* **6**, 1253–1254 (2003). doi:10.1038/nn1158 Medline

22. A. de Cheveigné, J.-M. Edeline, Q. Gaucher, B. Gourévitch, Component analysis reveals sharp tuning of the local field potential in the guinea pig auditory cortex. *J. Neurophysiol.* **109**, 261–272 (2013). doi:10.1152/jn.00040.2012 Medline

23. A. D. Redish, F. P. Battaglia, M. K. Chawla, A. D. Ekstrom, J. L. Gerrard, P. Lipa, E. S. Rosenzweig, P. F. Worley, J. F. Guzowski, B. L. McNaughton, C. A. Barnes, Independence of firing correlates of anatomically proximate hippocampal pyramidal cells. *J. Neurosci.* **21**, RC134 (2001). Medline

24. R. Schmidt, K. Diba, C. Leibold, D. Schmitz, G. Buzsáki, R. Kempter, Single-trial phase precession in the hippocampus. *J. Neurosci.* **29**, 13232–13241 (2009). doi:10.1523/JNEUROSCI.2270-09.2009 Medline

25. W. J. Freeman, B. Baird, Relation of olfactory EEG to behavior: spatial analysis. *Behav. Neurosci.* **101**, 393–408 (1987). doi:10.1037/0735-7044.101.3.393 Medline

26. K. Mizuseki, A. Sirota, E. Pastalkova, K. Diba, G. Buzsaki, Multiple single unit recordings from different rat hippocampal and entorhinal regions while the animals were performing multiple behavioral tasks (2013); available at http://crcns.org/data-sets/hc/hc-3

27. K. D. Harris, D. A. Henze, J. Csicsvari, H. Hirase, G. Buzsáki, Accuracy of tetrode spike separation as determined by simultaneous intracellular and extracellular measurements. *J. Neurophysiol.* **84**, 401–414 (2000). Medline

28. K. Mizuseki, A. Sirota, E. Pastalkova, G. Buzsáki, Theta oscillations provide temporal windows for local circuit computation in the entorhinal-hippocampal loop. *Neuron* **64**, 267–280 (2009). doi:10.1016/j.neuron.2009.08.037 Medline